

Preparation and Upconversion Luminescence of Three-Dimensionally Ordered Macroporous  $\text{ZrO}_2: \text{Er}^{3+}, \text{Yb}^{3+}$ Xuesong Qu,<sup>†</sup> Hongwei Song,<sup>\*‡</sup> Xue Bai,<sup>‡</sup> Guohui Pan,<sup>†</sup> Biao Dong,<sup>‡</sup> Haifeng Zhao,<sup>†</sup> Fang Wang,<sup>†</sup> and Ruifei Qin<sup>†</sup>

Key Laboratory of Excited State Physics, Changchun Institute of Optics, Fine Mechanics and Physics, Chinese Academy of Sciences, and Graduate school of Chinese Academy of Sciences, 16 Eastern Nan-Hu Road, Changchun 130033, P.R. China, and State Key Laboratory on Integrated Optoelectronics, College of Electronic Science and Engineering, Jilin University, Changchun 130012, P.R. China

Received April 1, 2008

The three-dimensionally ordered macroporous (3DOM)  $\text{ZrO}_2: \text{Er}^{3+}, \text{Yb}^{3+}$  materials were successfully synthesized by the sol–gel method combined with a polystyrene latex sphere templating technique, and their morphologies, surface physicochemical properties, and upconversion photoluminescence (UC-PL) properties were studied. The results indicate that the materials exhibited both porosity and strong UC-PL under the excitation of a 978 nm diode laser. In comparison with the nonporous samples, the relative intensity of the red ( ${}^4\text{F}_{9/2} \rightarrow {}^4\text{I}_{15/2}$ ) to the green ( ${}^4\text{S}_{3/2}/{}^2\text{H}_{11/2} \rightarrow {}^4\text{I}_{15/2}$ ) emission decreased visibly because of the decreased nonradiative relaxation in the 3DOM materials. It was also observed that the relative intensity of the green emission to the red emission increased significantly with the increasing excitation power. An indirect three-photon populating process occurred for the green emission as the excitation power and  $\text{Yb}^{3+}$  concentration was high enough.

## 1. Introduction

Several attractive features, such as large surface area and pore volume, tunable pore diameter, chemical inertness of porous oxide materials including micro-, meso- and macroporous, have attracted much attention because of their wide potential in catalytic properties, catalyst supports, and current or potential applications as adsorbents and hosts.<sup>1–7</sup> Further development of new multifunctional materials with porous structure is therefore of keen interest to enhance their

application to the desired areas. Among the novel multifunctional materials presently expected are ones combining the feature of not only “cavity” structure for the storage/delivery of specific species but also photoluminescence (PL) for simultaneous tracking or monitoring the species. Recently, many efforts have been devoted to preparing various photoluminescent nanostructures as mentioned above containing semiconductor quantum dots (QDs) and rare earth doped nanophosphors.<sup>4–7</sup> Shi et al. reported luminescent carbon nanotubes by depositing europium-doped  $\text{Y}_2\text{O}_3$  nanophosphors onto the surfaces of multiwalled carbon nanotubes.<sup>6</sup> More recently, Yang et al. synthesized a mesoporous SBA-15 silica based drug delivery system by depositing a  $\text{YVO}_4: \text{Eu}^{3+}$  nanophosphor layer on its surface, and the extent of drug release was identified by the change of luminescence.<sup>7</sup> In addition, three-dimensionally ordered macroporous (3DOM) materials, a new class of highly ordered porous materials, has been stimulating much interest because of their wide applications in adsorption, separation, catalysts, sensors, and photonic crystals.<sup>8–14</sup> Research on the 3DOM structure system of the luminescent matrix of semiconductors and rare

\* To whom correspondence should be addressed. E-mail: hwsong2005@yahoo.com.cn.

<sup>†</sup> Chinese Academy of Sciences, and Graduate school of Chinese Academy of Sciences.

<sup>‡</sup> Jilin University.

- (1) Kresge, C. T.; Leonowicz, M. E.; Roth, W. J.; Vartuli, J. C.; Beck, J. S. *Nature* **1992**, *359*, 710.
- (2) Yu, J.; Yu, J. C.; Leung, M. K.-P.; Ho, W.; Cheng, B.; Zhao, X.; Zhao, J. *J. Catal.* **2003**, *217*, 69.
- (3) Shchukin, D. G.; Caruso, R. A. *Adv. Funct. Mater.* **2003**, *13*, 789.
- (4) Lai, C. Y.; Trewyn, B. G.; Jeftinija, D. M.; Jeftinija, K.; Xu, S.; Jeftinija, S.; Lin, V. Y. *J. Am. Chem. Soc.* **2003**, *125*, 4451.
- (5) Sun, L. N.; Zhang, H. J.; Peng, C. Y.; Yu, J. B.; Meng, Q. G.; Fu, L. S.; Liu, F. Y.; Guo, X. M. *J. Phys. Chem. B* **2006**, *110*, 7249.
- (6) Shi, D.; Lian, J.; Wang, W.; Liu, G.; He, P.; Dong, Z.; Wang, L.; Ewing, R. C. *Adv. Mater.* **2006**, *18*, 189.
- (7) Zhang, L.; Yao, Y. Z.; Ye, X. F.; Wu, Q. *J. Phys. Chem. B* **2007**, *111*, 335.

(8) Holland, B. T.; Blanford, C. F.; Do, T.; Stein, A. *Chem. Mater.* **1999**, *11*, 795.

earth doped materials have been reported previously.<sup>11–13</sup> Yang et al.<sup>12</sup> recently reported the synthesis of  $\text{LaPO}_4: \text{Tb}$  inverse opal and studied the effect of the photonic stop-band on the spontaneous emission.

For mesoporous systems, although they combined the drug release with the PL label in one object, the PL nanoparticles were only grafted into the pore or on the surface by covalent/noncovalent bonding, even just by physical adsorption. The incomplete attachment and phase separation could make PL nanoparticles leach from the porous support during the process of the drug delivery and thus the changes of the PL intensity could not be a correct function of the released amount of the drug. So a porous material, generating PL itself, would be an ideal carrier for drug release. For a 3DOM structure, however, previous efforts only focus on the down-conversion luminescent materials, and few efforts have focused on the nanoscale upconversion photoluminescence (UC-PL) 3DOM structure to our knowledge.<sup>14</sup> UC-PL from near-infrared (NIR) to visible wavelength in materials doped with trivalent rare earth (RE) ions has attracted considerable interests because of their potential applications in three-dimensional displays, IR detection, and light emitting devices, biological labeling, and so on.<sup>15–18</sup> On the basis of the above considerations, in this paper we synthesized UC-PL  $\text{ZrO}_2: \text{Er}^{3+}, \text{Yb}^{3+}$  nanomaterials with 3DOM structure and studied their luminescence properties.  $\text{ZrO}_2$ , with its superior hardness, high refractive index, optical transparency, chemical stability, and photothermal stability, was chosen as an efficient UC-PL host for a 3DOM structure.<sup>19–21</sup> Because of the inherent structural and physical properties of the 3DOM structure, such as high surface area, 3D ordered macroporous structure, and the UC-PL properties, the present 3DOM structure of  $\text{ZrO}_2: \text{Er}^{3+}, \text{Yb}^{3+}$  materials is expected to achieve many applications.

## 2. Experimental Details

**2.1. Sample Preparation.** 3DOM  $\text{ZrO}_2: \text{Er}^{3+}$  (1 mol%),  $\text{Yb}^{3+}$  (2, 4, 8 mol%) were prepared by the sol–gel method combined with a polystyrene (PS) latex sphere templating technique. A monodisperse PS latex sphere was synthesized and packed into a

colloidal crystal by centrifugation for 24 h as described by Holland et al.<sup>8</sup> In the preparation of 3DOM  $\text{ZrO}_2: \text{Er}^{3+}, \text{Yb}^{3+}$ , appropriate amounts of  $\text{Er}(\text{NO}_3)_3$  and  $\text{Yb}(\text{NO}_3)_3$  were dissolved in ethanol under vigorous stirring, then added quickly to an ice-cooled solution of  $\text{Zr}(n\text{-OC}_4\text{H}_9)_4$ , and followed by further stirring for 30 min. Finally, the resulting mixed  $\text{ZrO}_2: \text{Er}^{3+}, \text{Yb}^{3+}$  sol (2 g) was dripped on PS (1 g) spheres, which were spread on a filter paper placed in a Büchner funnel while suction was applied. The resulting products were dried in air at room temperature for 24 h, then were elevated to 500 °C at a heating rate of 1.5 °C/min, and kept at 500 °C in air for 7 h. In this paper, three different dilution ratios (the molar ratio of the reactants  $\text{Zr}(n\text{-OC}_4\text{H}_9)_4$  to  $\text{C}_2\text{H}_5\text{OH}$ ) of 1:2, 1:5, and 1:9 were chosen to prepare the samples of 4 mol %  $\text{Yb}^{3+}$ . For comparison, the corresponding nonporous  $\text{ZrO}_2: \text{Er}^{3+}, \text{Yb}^{3+}$  materials were prepared and annealed by the same procedure without the PS colloidal templates.

**2.2. Measurements and Characterization.** X-ray diffraction (XRD) patterns of the samples were obtained with a Rigaku D/max-rA X-ray diffractometer with  $\text{Cu K}\alpha$  radiation. Fourier-transform infrared (FT-IR) spectra were measured by a Nexus 670 FT-IR spectrophotometer. Field emission scanning electron micrograph (FESEM) images were taken on a Hitachi S-4800 electron microscope. Thermogravimetric analysis (TGA) was performed on Perkin-Elmer Pyris Diamond thermogravimetric analyzer under nitrogen atmosphere at a heating rate of 10 °C/min. Brunauer–Emmett–Teller (BET) specific surface area and Barrett–Joiner–Halenda (BJH) pore size were calculated from nitrogen adsorption/desorption isotherms determined at –196 °C using an ASAP 2010 M surface analyzer (the samples were outgassed under vacuum at 200 °C). In upconversion luminescence (UCL) experiments, a 978 nm diode laser having a power maximum of 2 W was used to pump the samples. The visible emissions were collected using a Hitachi F-4500 fluorescence spectrometer.

## 3. Results and Discussion

**3.1. Crystal Structure and Morphology.** Figure 1 shows FESEM images of the PS (Figure 1A), 3DOM  $\text{ZrO}_2: \text{Er}^{3+}, \text{Yb}^{3+}$  (Figure 1B–H), and the nonporous sample (Figure 1I). As-prepared PS latex spheres are monodisperse, and their particle sizes are uniform with the average diameter of 400 nm (see Figure 1A). It can be seen from Figure 1 B–H that the 3DOM materials exhibit close packed and three-dimensional ordering of pores similar to that of the PS template and that no residual PS particles and excess inorganic materials exist. Furthermore, the pores are interconnected through windows resulting from the contact between the template (PS) spheres prior to infiltration of the precursor solution, and the material exhibits multilayer structure. The  $\text{ZrO}_2: \text{Er}^{3+}, \text{Yb}^{3+}$  nanoparticles aggregate on their wall with a homogeneous particle size distribution and constitute a skeleton surrounding the uniform close-packed round-shaped macropores. Note that the morphology including the wall thickness, average pore diameter, and ordering of the pores of the products was strongly related to the concentration of the precursors because the viscosity and hydrolysis/condensation rate of the precursors was affected by the concentration. The SEM images in the panels B–H in Figure 1 depict the changes in wall thickness and ordering of the macropores for products obtained at various dilution ratios. When the dilution ratio was 1:2, well-ordered macroporous structures were obtained, and the average pore

- (9) Wang, C.; Geng, A.; Guo, Y.; Jiang, S.; Qu, X.; Li, L. *J. Colloid Interface Sci.* **2006**, *301*, 236.
- (10) Melde, B. J.; Stein, A. *Chem. Mater.* **2002**, *14*, 3326.
- (11) Lodahl, P.; VanDriel, A. F.; Nikolaev, I. S.; Overgaag, A. I.; Vanmaekelbergh, D.; Vos, W. L. *Nature* **2004**, *430*, 654.
- (12) Romanov, S. G.; Fokin, A. V.; De, L.; Rue, R. M. *Appl. Phys. Lett.* **2000**, *76*, 1656.
- (13) Yang, Z.; Zhou, J.; Huang, X.; Yang, G.; Xie, Q.; Sun, L.; Li, B.; Li, L. *Chem. Phys. Lett.* **2008**, *455*, 55.
- (14) Jeon, S.; Braun, P. V. *Chem. Mater.* **2003**, *15*, 1256.
- (15) Sun, H.; Dai, S.; Xu, S.; Zhang, J.; Hu, L.; Jiang, Z. *Physica B* **2004**, *352*, 366.
- (16) Heer, S.; Kömpe, K.; Güdel, H.-U.; Haase, M. *Adv. Mater.* **2004**, *16*, 2102.
- (17) Yi, G. S.; Lu, H. C.; Zhao, S.; Ge, Y.; Yang, W. J.; Chen, D.; Guo, L. H. *Nano Lett.* **2004**, *4*, 2191.
- (18) Wang, L. Y.; Yan, R. X.; Huo, Z. Y.; Wang, L.; Zeng, J. H.; Bao, J.; Wang, X.; Peng, Q.; Li, Y. D. *Angew. Chem., Int. Ed.* **2005**, *44*, 6054.
- (19) Chen, G.; Somesfalean, G.; Liu, Y.; Zhang, Z.; Sun, Q.; Wang, F. *Phys. Rev. B* **2007**, *75*, 195204.
- (20) Patra, A.; Friend, C. S.; Kapoor, R.; Prasad, P. N. *J. Phys. Chem. B* **2002**, *106*, 1909.
- (21) De la Rosaa, E.; Salas, P.; Desirena, H.; Angeles, C.; Rodríguez, R. A. *Appl. Phys. Lett.* **2005**, *87*, 241912.

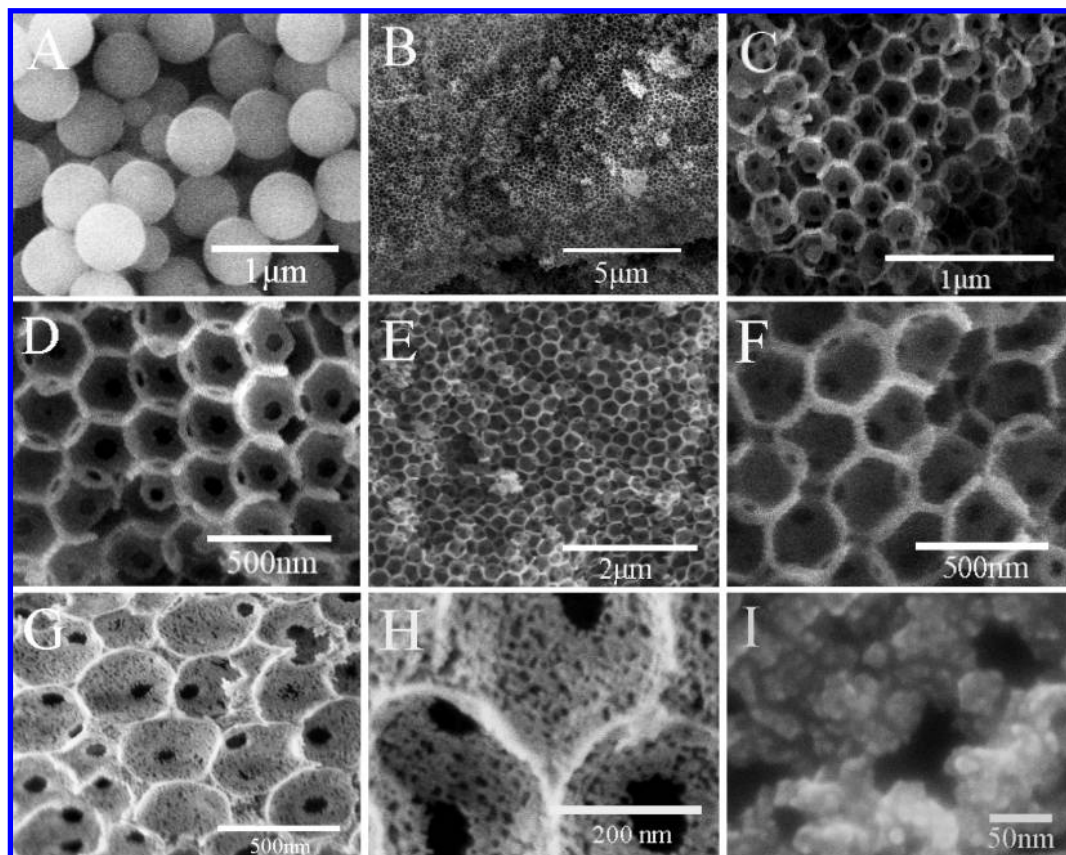


**Figure 1.** FESEM images of as-prepared (A) PS; (B–D) 3DOM  $\text{ZrO}_2: \text{Er}^{3+}, \text{Yb}^{3+}$  with dilution ratios of 1:2; (E, F) 3DOM  $\text{ZrO}_2: \text{Er}^{3+}, \text{Yb}^{3+}$  with the dilution ratios of 1:5; (G, H) 3DOM  $\text{ZrO}_2: \text{Er}^{3+}, \text{Yb}^{3+}$  with the dilution ratios of 1:9; (I) SEM image of the nonporous  $\text{ZrO}_2: \text{Er}^{3+}, \text{Yb}^{3+}$ .

diameter, interconnected window diameter, wall thickness, and particle size were estimated to be  $\sim 220$ , 70, 35 and 10 nm, respectively. When further diluting the zirconium alkoxide precursor with alcohol to the dilution ratios of 1:5 and 1:9, structural defects increased and disordered structures were formed, as shown in Figure 1 E–H. At the same time, the wall thickness decreased to 25 and 10 nm, respectively. Dilution in ethanol resulted in the formation of less ordered structures and a thinner wall. It has been reported that, at higher dilution, the ethanol may have partially dispersed the colloidal latex crystal, causing the decrease in order for the products.<sup>8</sup> In the present work, the well-ordered structures were obtained at the dilution ratio of 1:2. The decreased pore diameters of 3DOM materials compared with the PS templates are due to the shrinkage during the process of calcinations and the shrinkage decrease as the dilution ratios increase. The average pore diameter increased from 220 to 260 and 320 nm when the dilution ratio changed to 1:5 and 1:9. From Figure 1I, it can be observed that the nonporous sample yields nanoparticles with an average size of 10 nm and the particles tend to aggregate together. From the results above, we suggest that the fabrication of a 3DOM structure could make the  $\text{ZrO}_2: \text{Er}^{3+}, \text{Yb}^{3+}$  nanocrystals (NCs) dispersed better, and it is possible to control the average pore diameter and wall thickness by adjusting the dilution ratios in a certain range.

Figure 2 displays the XRD patterns of the 3DOM  $\text{ZrO}_2$  and  $\text{ZrO}_2: \text{Er}^{3+}, \text{Yb}^{3+}$  with different doping concentrations of  $\text{Yb}^{3+}$  ions. According to the JCPDS standard cards, all

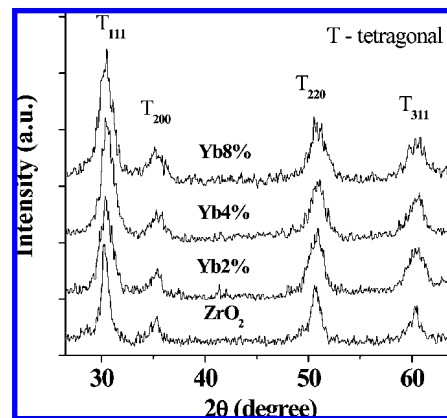


**Figure 2.** XRD patterns of 3DOM  $\text{ZrO}_2$  and  $\text{ZrO}_2: \text{Er}^{3+}, \text{Yb}^{3+}$  composites.

the samples exhibit tetragonal phase with the characteristic  $2\theta$  values at  $30.1^\circ$  (111),  $35.2^\circ$  (200),  $50.4^\circ$  (220), and  $59.9^\circ$  (311), respectively (JCPDS file 17-0923). On the basis of the Scherrer equation, the average crystalline size is estimated to be 9 nm, which is nearly identical with that observed by SEM images. In comparison with the pure  $\text{ZrO}_2$ , the XRD peaks in the  $\text{ZrO}_2: \text{Er}^{3+}, \text{Yb}^{3+}$  3DOM materials shift a little to the large diffraction angle, implying that the lattice constants become smaller.

Figure 3 shows the FTIR spectra of the 3DOM  $\text{ZrO}_2: \text{Yb}^{3+}, \text{Er}^{3+}$ , the corresponding nonporous materials, and the PS samples. There is no mode related to PS appearing in the 3DOM sample, further implying that the PS template was

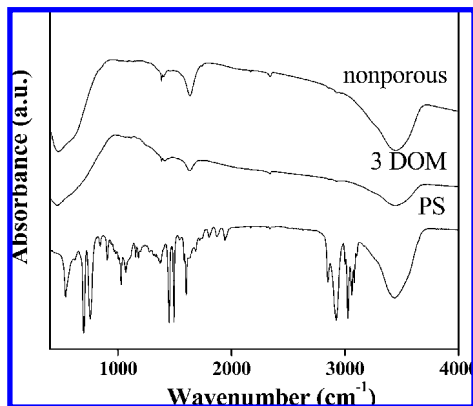


**Figure 3.** FTIR spectra of as-prepared PS, 3DOM  $\text{ZrO}_2: \text{Er}^{3+}$  (1%),  $\text{Yb}^{3+}$  (4%), and the corresponding nonporous materials.

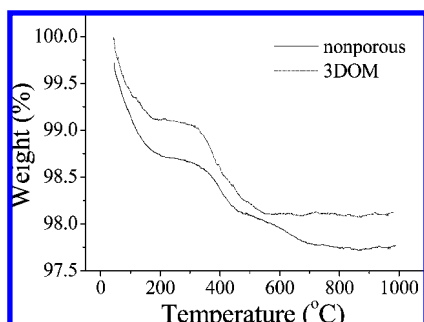


**Figure 4.** TGA trace obtained at 10 °C/min under flowing  $\text{N}_2$  of as-prepared 3DOM  $\text{ZrO}_2: \text{Er}^{3+}$  (1%),  $\text{Yb}^{3+}$  (4%), and the corresponding nonporous materials.

removed completely after calcination at 500 °C. The 3DOM and nonporous samples both exhibit four peaks in the measured range, locating at 470, 1380, 1635, and 3450  $\text{cm}^{-1}$ , respectively. The 470  $\text{cm}^{-1}$  band is assigned to the Zr–O vibration, and the 1380  $\text{cm}^{-1}$  band can be attributed to very small amounts of *n*-BuOH originating from the resource of Zr.<sup>22</sup> The bands located at 1635 and 3450  $\text{cm}^{-1}$  are assigned to the –OH bending and stretching modes, respectively, corresponding to the surface contamination with water. It is obvious that the surface adsorption of water in the 3DOM sample becomes much less in contrast to that in the nonporous sample. To further determine the amount of surface adsorption water in these two samples, a TGA experiment was performed. As displayed in Figure 4, there was about 2.3% weight loss assigned to the desorption of water and residual solvent from room temperature to 750 °C and little weight loss after that in the nonporous sample. However, 1.9% weight loss was observed for the 3DOM sample, and the temperature at which weight losses essentially ended shifted to lower values (590 °C) compared with 750 °C in the nonporous sample. It indicated that the 3DOM structure was benefited by the removal of the surface adsorption, and the result also confirmed that adsorption water in the 3DOM sample was less (0.4 wt %) in contrast to that in the nonporous sample. The 3DOM sample was obtained by permeating  $\text{ZrO}_2: \text{Er}^{3+}, \text{Yb}^{3+}$  sol into the interstices between PS latex spheres and removing the PS template by

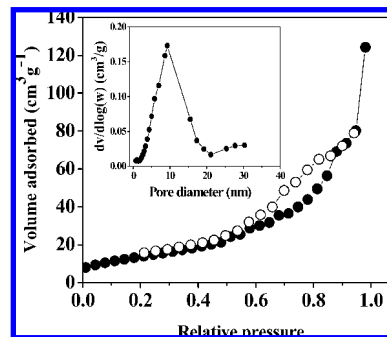


**Figure 5.**  $\text{N}_2$  adsorption/desorption isotherms and pore size distribution curves (inset) of as-prepared 3DOM  $\text{ZrO}_2: \text{Er}^{3+}$  (1%),  $\text{Yb}^{3+}$  (4%).

calcinations. PS templates combusted and decomposed with the increasing temperature, and the process was exothermic. Thus, the surface contamination was easily removed compared with the nonporous sample. Meanwhile, the macroporous structure makes the calcinations more effective because of the void volume available to exhale. The decrease of surface adsorption of water can lead to the decrease of nonradiative relaxation of  $\text{Er}^{3+}$  and the increase of UC efficiency.<sup>16,23</sup>

**3.2. Surface Physicochemical Properties.** The surface physicochemical properties of the as-prepared macroporous  $\text{ZrO}_2: \text{Er}^{3+}$  (1%),  $\text{Yb}^{3+}$  (4%) obtained at the dilution ratio of 1:5 (as a typical example) was characterized by  $\text{N}_2$  adsorption/desorption analyses, as shown in Figure 5. It is obvious that the isotherms exhibit hysteresis behaviors, indicating that the walls of macroporosity are mainly mesoporous. The average pore size calculated by the BJH method is 9.1 nm, which is consistent with the result of the SEM images. Formation of the mesopores among the wall of the composites was due to the aggregation of the particles during the hydrolysis process of the precursor solution, which was also observed in the alkoxide-based sol–gel products.<sup>9,24</sup> The calculated BET specific surface area and pore volume are 69.30  $\text{m}^2/\text{g}$  and 0.1891  $\text{cm}^3/\text{g}$ , respectively. Because of the existence of macroporous morphology with a hollow structure with inner diameters of the order of 200 nm and a mesoporous wall, anticipated applications may be achieved in this system.

**3.3. UCL Spectra of  $\text{ZrO}_2: \text{Er}^{3+}, \text{Yb}^{3+}$ .** Figure 6 shows the UC-PL spectra of 3DOM  $\text{ZrO}_2: \text{Er}^{3+}, \text{Yb}^{3+}$  with various concentrations of  $\text{Yb}^{3+}$  ions and the corresponding nonporous samples under the 978 nm excitation. In the spectra the green emissions in the range of 500–580 nm correspond to the  ${}^2\text{H}_{11/2}, {}^4\text{S}_{3/2} \rightarrow {}^4\text{I}_{15/2}$  transitions, while the red lines between 640 and 690 nm correspond to the  ${}^4\text{F}_{9/2} \rightarrow {}^4\text{I}_{15/2}$  transitions in both the 3DOM and the nonporous samples. The blue emissions of  ${}^2\text{H}_{9/2} \rightarrow {}^4\text{I}_{15/2}$  can be also observed as the  $\text{Yb}^{3+}$  concentration and the excitation power is high enough. It can be observed that the ratio of the red emissions  ${}^4\text{F}_{9/2} \rightarrow {}^4\text{I}_{15/2}$  to the green emissions  ${}^4\text{S}_{3/2}/{}^2\text{H}_{11/2} \rightarrow {}^4\text{I}_{15/2}$  increases with the increasing  $\text{Yb}^{3+}$  concentration. Similar results have also been observed in the  $\text{Er}^{3+}$  and  $\text{Yb}^{3+}$  co-doped  $\text{Y}_2\text{O}_3$  and  $\text{Gd}_2\text{O}_3$  NCs, and they have been well explained according

(22) Gedanken, A.; Reisfeld, R.; Sominski, E.; Palchik, O.; Koltypin, Y.; Panczer, G.; Gaft, M.; Minti, H. *J. Phys. Chem. B* **2000**, *104*, 7057.

(23) Capobianco, J. A.; Vetrone, F.; D'Alesio, T.; Tessari, G.; Spighini, A.; Bettinelli, M. *Phys. Chem. Chem. Phys.* **2000**, *2*, 3203.

(24) Qu, X.; Guo, Y.; Hu, C. *J. Mol. Catal. A: Chem.* **2007**, *262*, 128.

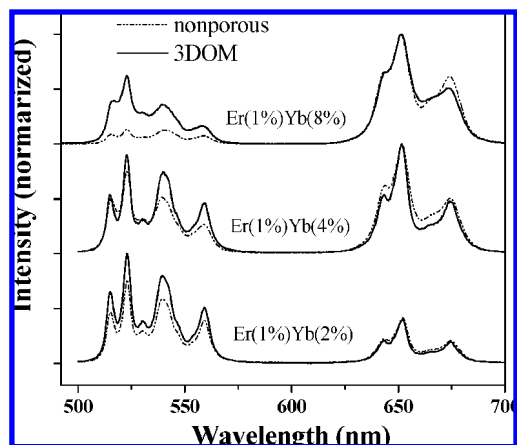


**Figure 6.** UC-PL spectra of 3DOM  $\text{ZrO}_2:\text{Er}^{3+}, \text{Yb}^{3+}$  and the corresponding nonporous materials under 980 nm excitation ( $I_{\text{ex}} = 0.989 \text{ W/mm}^2$ ).

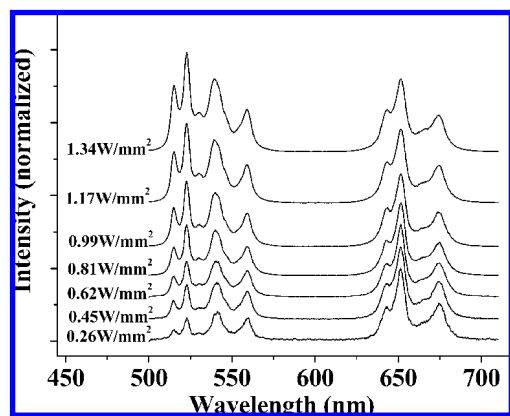


**Figure 7.** UC-PL spectra of various  $\text{ZrO}_2:\text{Er}^{3+} (1\%), \text{Yb}^{3+} (4\%)$  under 980 nm excitation with different power density (the red emissions at 651 nm were normalized).

to the phenomenon of cross relaxation.<sup>25,26</sup> In contrast to the nonporous samples, the green emissions in the 3DOM sample increase relative to the red emissions. On the basis of the FTIR spectra and TGA, the 3DOM sample adsorbed less water in comparison to the nonporous one. This led the nonradiative relaxation of  ${}^4I_{11/2} \rightarrow {}^4I_{13/2}$  for  $\text{Er}^{3+}$  to decrease, and as a result, the population of the red level decreased and that of the green level increased. The UC mechanism in the oxide NCs has been studied previously.<sup>27</sup>

**3.4. Power-Dependence of UCL and Population Processes.** Figure 7 shows the UC-PL spectra of  $\text{ZrO}_2:\text{Er}^{3+} (1\%), \text{Yb}^{3+} (4\%)$  under the excitation with different powers. It is apparent that the intensity ratio of the green emission to the red emission increased with the increasing excitation power. As shown in the Figure 7, the red emission is stronger than the green one when the excitation power is lower, and the green emission surpassed the red one when the excitation power is higher. A similar phenomenon was observed in the other  $\text{Er}^{3+}$  and  $\text{Yb}^{3+}$  co-doped oxide NCs such as  $\text{Y}_2\text{O}_3$ <sup>23</sup>

(25) Ventrone, F.; Boyer, C.; Capobianco, J. A. *J. Appl. Phys.* **2004**, *96*, 661.

(26) Lei, Y.; Song, H.; Yang, L.; Yu, L.; Liu, Z.; Pan, G.; Bai, X.; Fan, L. *J. Chem. Phys.* **2005**, *123*, 174710.

(27) Song, H. W.; Sun, B. J.; Wang, T.; Lu, S. Z.; Yang, L. M.; Chen, B. J.; Wang, X. J.; Kong, X. G. *Solid. State. Commun.* **2004**, *132*, 409.

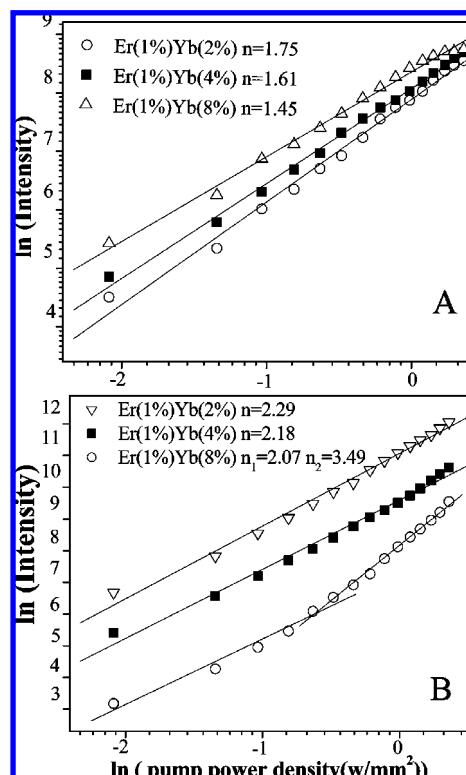


**Figure 8.** In-ln plot of the emission intensity as a function of the excitation power density for (A) the red emission and (B) the green emission.

and  $\text{Gd}_2\text{O}_3$ <sup>24</sup> and was also theoretically described by Pollnau et al.<sup>28</sup> This behavior fundamentally derives from the competitive mechanisms of UC and linear decay for the depletion of the intermediate excited state. The intermediate excited state of the green emission is  ${}^4I_{11/2}$ , while that of the red emission is  ${}^4I_{13/2}$ . With increasing pump power and the resulting increasing importance of UC, UC ( ${}^4I_{11/2} \rightarrow {}^4F_{7/2}$ ) dominates over linear decay ( ${}^4I_{11/2} \rightarrow {}^4I_{13/2}$ ) for the depletion of the  ${}^4I_{11/2}$  level; hence, the ratio of the green emission to the red emission increases with the increase of excitation power.

Panels A and B of Figure 8 show, respectively, the In-ln plots of the emission intensity as a function of excitation power for the red and green emissions. As is well-known, for any UC mechanism the visible output power intensity ( $I_v$ ) will be proportional to some power ( $n$ ) of the infrared excitation ( $I_{\text{IR}}$ ) power if the saturation effect can be neglected:<sup>28,29</sup>  $I_{\text{PL}} \propto I_{\text{ex}}^n$ , where  $n$  is the number of IR phonons absorbed per visible phonon emitted. In the In-ln plots, the values of  $n$  for the red emissions were determined to be 1.75, 1.61, and 1.45, respectively, in the samples of 2, 4, and 8 mol %  $\text{Yb}^{3+}$ . Two-photons are involved for populating the red emission levels and the value of  $n$  decreased with increasing  $\text{Yb}^{3+}$  concentration in the range of 1–2. This can be attributed to the competition between linear decay and UC processes.<sup>25</sup> For the green emissions, the values of  $n$  were determined to be 2.29 and 2.18 in the samples of 2 and 4 mol %  $\text{Yb}^{3+}$ , and in the sample of 8 mol %  $\text{Yb}^{3+}$ , the slope

(28) Pollnau, M.; Gamelin, D. R.; Lüthi, S. R.; Güdel, H. U.; Hehlen, M. P. *Phys. Rev. B* **2000**, *61*, 3337.

(29) Chamarro, M. A.; Cases, R. *J. Lumin.* **1990**, *46*, 59.

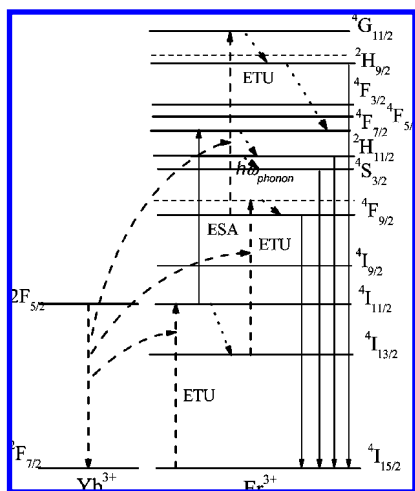


**Figure 9.** Energy-level diagram of  $\text{Yb}^{3+}$ ,  $\text{Er}^{3+}$  co-doped samples and possible UC-PL processes under 980 nm excitation. ESA and ETU are the representations of excited-state absorption and energy-transfer UC, respectively.

$n$  was found to be 2.07 under the lower excitation power and 3.49 under the higher power. This indicates that the green emissions usually originate from a two-photon populating process; however, as the excitation power and  $\text{Yb}^{3+}$  concentration is high enough, they come from an indirect three-photon populating process. The three-photon populating process for the green emissions was also observed in  $\text{Er}^{3+}/\text{Yb}^{3+}$  co-doped  $\text{Y}_2\text{O}_3$  NCs, as well as from the phosphate glasses.<sup>27,30</sup> The existence of large vibration modes in the host is a key factor for generating the three-photon populating

process for the green level. Because the UC-PL and relaxation processes are very complicated, we could not provide the mechanism according to the presented results. In accordance with previous studies,<sup>27,28,30</sup> the mechanisms shown in Figure 9 would be consistent with the experimental observations.

#### 4. Conclusions

In summary, UC-PL  $\text{ZrO}_2$ :  $\text{Er}^{3+}$ ,  $\text{Yb}^{3+}$  materials exhibiting macro-mesoporous structure were successfully designed and prepared. By adjusting the viscosity of the reactants and the pore diameter, we controlled the wall thickness and the window sizes of this material. Moreover, in contrast to the nonporous materials, the UC-PL properties were improved because of less surface adsorption of water. Because of the competitive mechanisms of UC and linear decay for the depletion of the intermediate excited state, the relative intensity of the green emission to the red emission increased significantly with the increasing excitation power. A three-photon excitation was involved in the UC mechanism responsible for populating the green level as the  $\text{Yb}^{3+}$  concentration and the pumping power were high enough. The materials not only provide macro-mesoporosity but also exhibit attractive UC-PL properties, which confer on them multifunctional application in several fields.

**Acknowledgment.** This work is financial supported by the financial supports of Nation Natural Science Foundation of China (Grants 50772042, 10704073, and 10504030) and the 863 Project of China (2007AA032314).

(30) Song, F.; Zhang, G.; Shang, M.; Tan, H.; Yang, J.; Meng, F. *Appl. Phys. Lett.* **2001**, *79*, 1748.